Received 1 July 2024; accepted 16 August 2024. Date of publication 21 August 2024; date of current version 30 August 2024.
The review of this article was arranged by Editor G. Malavena.

*Digital Object Identifier 10.1109/JEDS.2024.3447149*

# Discrete-Trap Effects on 3-D NAND Variability – Part I: Threshold Voltage

**GERARDO MALAVENA[1] (Member, IEEE), SALVATORE M. AMOROSO[2], ANDREW R. BROWN[2], PLAMEN ASENOV[2], XI-WEI LIN[2] (Member, IEEE), VICTOR MOROZ[2], MATTIA GIULIANINI[1], DAVID REFALDI[1], CHRISTIAN MONZIO COMPAGNONI[1] (Senior Member, IEEE), AND ALESSANDRO S. SPINELLI[1] (Senior Member, IEEE)**

1 Dipartimento di Elettronica, Informazione e Bioingegneria, Politecnico di Milano, 20133 Milan, Italy
2 Synopsys Inc., Mountain View, CA 94043, USA

CORRESPONDING AUTHOR: G. MALAVENA (e-mail: gerardo.malavena@polimi.it)

**ABSTRACT** In this two-part article we discuss the difference between a continuous and a discrete approach to trap modeling in the simulation of 3-D NAND Flash memories with polysilicon channel. In Part I we focus on threshold voltage ($V_T$) fluctuations induced by traps and show that lower values for the average and rms $V_T$ arise when the discrete nature of traps is accounted for. We explain such differences in terms of a stronger percolation that leads to a lower number of filled traps in the discrete-trap case, and investigate such differences as a function of cell parameters and temperature. Finally, we compare the two approaches showing that a continuous trap model cannot reproduce the correct dependences resulting from a discrete treatment.

**INDEX TERMS** 3D NAND Flash memories, variability, discrete traps.

## I. INTRODUCTION

The successful exploitation of the vertical dimension by the NAND Flash technology has resulted in an unprecedented increase in performance [1], [2], with current chips reaching more than 300 layers [3] and adopting a five-bits-per-cell technology [4]. The need to accurately control the electrical characteristics of billions of devices becomes a formidable reliability challenge [5], where variability effects play a key role.

A number of different factors affects the spread in device parameters, such as geometric variations [6], [7], [8], [9] and intrinsic fluctuations due to the polycrystalline nature of the vertical silicon channel, where traps in highly-defective grain boundaries (GBs) can influence the carrier transport. Several works have demonstrated the role of the GBs in the string conduction of 3-D NAND cells, pointing out their impact on both the threshold voltage ($V_T$) and its spread [10], [11], [12], [13], [14], [15], [16], [17], and on random telegraph noise (RTN), *i*.e., $V_T$ fluctuations due to a single-electron capture in a trap [18], [19], [20], [21],[22], [23].

Numerical simulation is a powerful tool to investigate the above-mentioned issues and understand the physical phenomena involved. However, simulations are usually carried out relying on a continuous distribution of traps, although trap discretization is expected to play a non-negligible role in the assessment of $V_T$ and its fluctuations, in the same way as dopant discretization turned out to be fundamental in assessing such quantities in crystalline devices. Yet, only a few works adopted this approach [12], [14], [18], [20], and a thorough comparison between results obtained with a discrete and a continuous treatment of traps is still missing, particularly as a function of physical and architectural parameters. This is the purpose of this work: we discuss the impact of trap discretization on $V_T$ and RTN, and investigate its dependence on different cell parameters. The work is broken down into two parts: Part I deals with $V_T$ fluctuations, while Part II [24] discusses RTN. Preliminary results of this work have been presented in [25]; here we expand the physical analysis and add the dependence on device parameters and temperature. Results of this work make clear that a full discrete-trap approach is required to correctly calibrate the physical parameters of device simulation and develop reliable tools for accurate variability prediction.

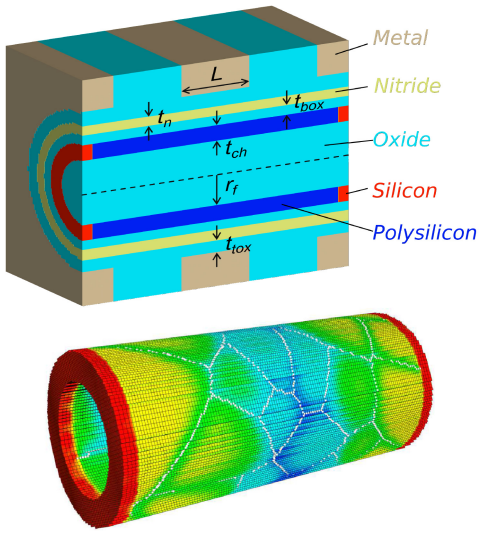


**FIGURE 1.** **Top: Schematic of the Macaroni device structure. Relevant device parameters are $L = 35$ nm, $t_{ch} = 10$ nm, $t_n = t_{box} = 6$ nm, $t_{tox} = 8$ nm, $r_f = 20$ nm. Bottom: Example of granular polysilicon structure generated by Garand VE. Colors refer to the electron density (blue = low; red = high).**

## II. SIMULATION FRAMEWORK

We focused on a 3D NAND architecture where cylindrical strings run vertically from a sourceline to a bitline, while planar wordlines define the control gates of the memory cells. The structure consists of a central cell whose $V_T$ is measured, with the addition of two half-cells per side, in order to correctly capture possible fringing field effects, as depicted in Fig. 1. We employed a Macaroni cell [26] with radial structure made of a filler oxide (radius $r_f$), a thin layer of polysilicon (thickness $t_{ch}$), an oxide/nitride/oxide stack (thicknesses $t_{box}/t_n/t_{tox}$), and a metal wordline (WL). Cell and inter-cell length is $L$. Parameter values are also listed in Fig. 1.

3-D Monte Carlo simulations were performed using Sentaurus Process [27] and Sentaurus Device [28] for processing the typical cell structure and Garand VE [29] for studying the statistical behavior of the cell. The stochastic nature of polycrystalline silicon is taken into account by means of random grains having average size $D_g = 30$ nm and traps located at their GBs. As the purpose of our work is not to fit any experimental data, but rather to discuss the impact of trap discretization, we selected typical parameter values from literature [10], [19], [30], adopting a double-exponential trap energy distribution $D$ of acceptor-like traps in the GB energy gap

$$D(E) = D_t\ e^{(E-E_C)/E_t} + D_d\ e^{(E-E_C)/E_d}, \qquad (1)$$

where $D_t = 3.53 \times 10^{15}$ cm$^{-2}$ eV$^{-1}$ and $D_d = 7.16 \times 10^{12}$ cm$^{-2}$ eV$^{-1}$ are tail and deep state densities, $E$ and $E_C$ are the energy and the conduction band edge, $E_t = 16.6$ meV, $E_d = 160.6$ meV. These values are derived from the bulk trap distribution in [30], and give the same average number of traps in the device volume for our reference case. Donor-like states have been neglected for simplicity, while the effect of a constant polysilicon/oxide interface state density of average value $10^{11}$ cm$^{-2}$ eV$^{-1}$ will also be considered. Finally, the actual number of traps in the GBs and oxide interfaces are drawn from Poisson distributions given the previous average values. Traps are then allocated either as discrete entities, as in [31], or as continuous entities [10], [19]. It is worth stressing that a continuous distribution function is still used for computing the discrete trap occupancy, so to avoid oscillations in steady-state results when a trap energy falls exactly at the Fermi level.

Carrier transport in the polysilicon channel is solved by means of drift-diffusion equations with density-gradient corrections to account for quantum effects at the silicon-oxide interfaces and GBs. To focus on percolation and electrostatic effects, a low bitline bias of 50 mV and a constant mobility $\mu_n = 100$ cm$^2$ V$^{-1}$ s$^{-1}$ are also adopted. The voltage applied to the WLs of the lateral cells was always kept at 6 V, to make them act as pass-transistors, while $V_T$ is defined as the central-WL bias that grants a current $I_T = 10$ nA (except where noted). In the following, we label $V_{TC}$ and $V_{TD}$ the $V_T$ values extracted following a continuous-trap (CT) and discrete-trap (DT) approach, respectively.

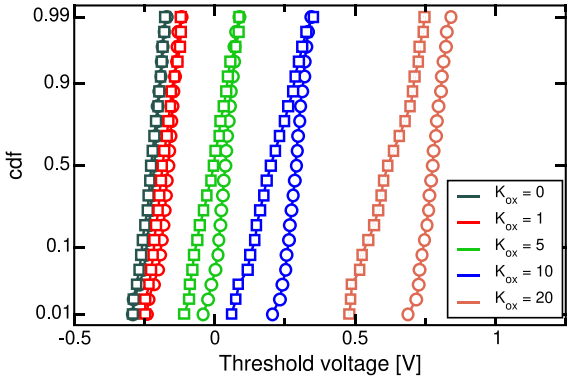


**FIGURE 2.** **$V_T$ cdf for different values of the polysilicon/oxide interface trap density. Circles = CTs, squares = DTs.**

## III. SIMULATION RESULTS

### A. POLYSILICON/OXIDE INTERFACE TRAPS

We begin our analysis by focusing on polysilicon/oxide interface traps, comparing the two approaches as a function of the trap density. Fig. 2 shows the $V_T$ cumulative distribution function (cdf) when the average value of the polysilicon/oxide interface trap density is multiplied by a factor $K_{ox}$. Both CT and DT distributions shift with $K_{ox}$, as expected, but their shape is quite different: the rms $V_{TC}$ value is very small (in the 20 mV range) and almost independent of $K_{ox}$, and is only due to the Poisson fluctuation in the (uniform) trap density. A DT approach results first of all in a marked reduction in the impact of $K_{ox}$: as it changes from 0 to 20, the average $V_{TD}$ shifts by 600 mV, as opposed to 750 mV for $V_{TC}$. The rms $V_{TD}$, instead, increases up to about 65 mV.

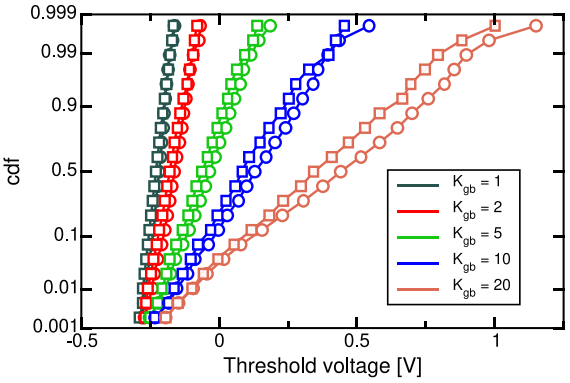


**FIGURE 3.** $V_T$ cdf for different values of the GB trap density. Circles = CTs, squares = DTs.

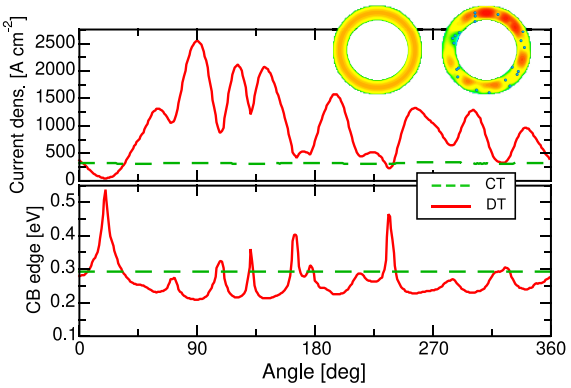


**FIGURE 4.** Conduction band edge (bottom) and current density (top) at the GB position of a single-radial-grain device as a function of the angle, for the CT and DT cases. Top figures show color maps of the current densities at the GB for the CT (left) and DT (right) cases.

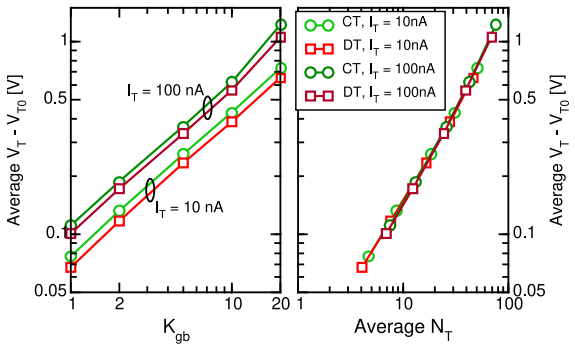


**FIGURE 5.** Average $V_T$ difference as a function of the GB trap density (left) and the average $N_T$ (right). Circles = CTs, squares = DTs.

Such differences are consequences of DT localization, leading to non-uniformity in the inversion channel: electrons will flow away from charged DTs, decreasing their effect on $V_T$. The additional degree of freedom enjoyed by DT positions in space and energy also explains the higher spread in $V_{TD}$, and means that a crossover between the cdfs at the high $V_T$ end is expected (see for example the green and blue curves): these are the cells whose DTs happen to be strongly localized in the channel, increasing $V_{TD}$.

### B. GRAIN BOUNDARY TRAPS

We then investigated the $V_T$ dependence on the GB traps, scaling their densities by a factor $K_{gb}$, still in the $1-20$ range. Before presenting the results, two comments are necessary: First, as the reference tail state areal density $D_t E_t \approx 6 \times 10^{13}$ cm$^{-2}$ is already significant, a concern might be raised about the physical soundness of devices at the high $K_{gb}$ limit. Such a discussion will be deferred to the Appendix, so not to interrupt the analysis of the results. Second, the previous results have shown that interface traps can affect the $V_T$ average and rms values, becoming dominant for low $K_{gb}$ values. In order to extract the correct dependences, we then removed the interface state density from the following simulations.

The $V_T$ cdfs for different values of $K_{gb}$ are shown in Fig. 3, and feature some interesting differences from Fig. 2: now both $V_{TC}$ and $V_{TD}$ average value and spread increase with $K_{gb}$, with lower values for $V_{TD}$. So, the cdfs show no crossover at the high-$V_T$ side, but similar behaviors at the low-probability end, where GB traps have little effect on $V_T$. Let us begin the analysis of the results by focusing on the $V_T$ difference: to gain some insight, we simulated a simple cell having just one GB placed orthogonally to the Macaroni cylindrical axis, and located at mid-channel position. Fig. 4 shows the results for $E_c$ and current density at the GB position, as a function of the rotation angle and for the same WL bias. In the CT case, a uniform profile is obtained, as expected. In the DT case, instead, $E_c$ features sharp 3-D Coulomb peaks in correspondence of the discrete filled traps, and large valleys away from such spots. Because of the exponential dependence between electron concentration (hence, current) and $E_c$, the net effect is to increase the total current for a given bias, *i.e.*, give a lower $V_T$. This non-linear effect of traps on the current explains why it is not possible to regard the CT framework simply as an average of many DT simulations. The random trap positions and resulting current profile are also pictorially shown in the two cross-sections at the top: note the non-uniform profile on the right (DT case) as opposed to the uniform CT case (left).

The effect of trap discretization can be best appreciated if we focus on the increment in the average $V_T$ with respect to the $K_{gb} = 0$ case ($V_{T0}$). Such quantity is reported in Fig. 5 (left) as a function of $K_{gb}$: $V_{TC}$ and $V_{TD}$ follow the same 0.75 power-law dependence, with a reduction in the average shift by about 12% for DTs. The Figure also shows data extracted at $I_T = 100$ nA, where the same dependence is also obtained. Fig. 5 (right) shows instead the same quantities as a function of the average number of filled traps in the channel, $N_T$: note that a single behavior (power-law with slope 0.92) is obtained irrespective of $I_T$ and the approach adopted, suggesting that $N_T$ is the key parameter controlling $V_T$, and that the stronger DT percolation results in a lower $V_{TD}$, hence a smaller $N_T$.

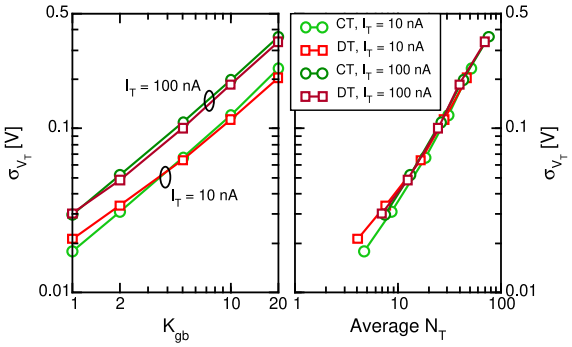


**FIGURE 6.** Rms $V_T$ as a function of the GB trap density (left) and of the average $N_T$ (right). Circles = CTs, squares = DTs.

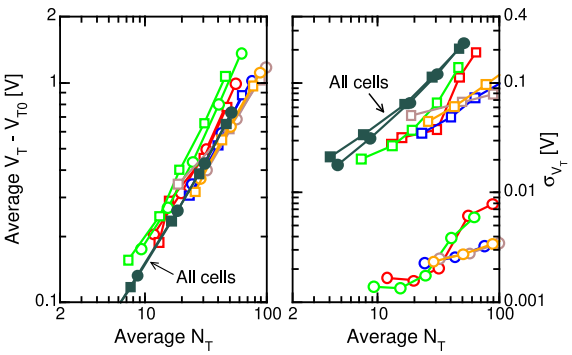


**FIGURE 7.** Data in Figs. 5 and 6 (for $I_T = 10$ nA only) as a function of the average $N_T$ (black) with the addition of five random cells with fixed GB configuration (other colors). Circles = CTs, squares = DTs.

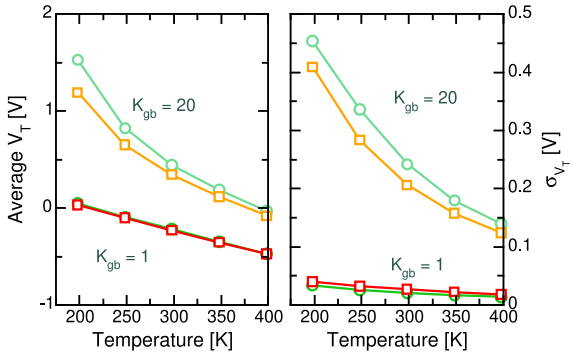


**FIGURE 8.** Average and rms $V_T$ values as a function of temperature for $K_{gb} = 1$ and 20. Circles = CTs, squares = DTs.

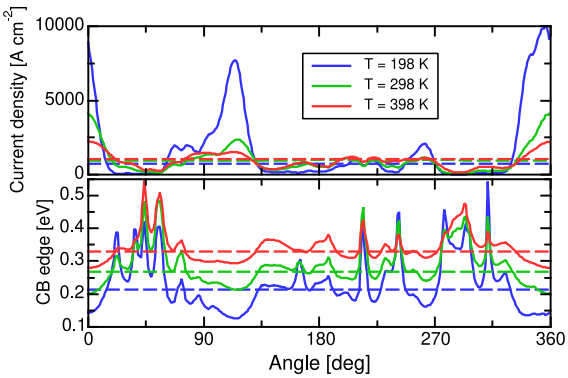


**FIGURE 9.** Same as Fig. 4, but different random traps and with temperature ranging from 198 to 398 K. Solid lines = DTs, dashes = CTs.

Fig. 6 shows the rms $V_T$ ($\sigma_{V_T}$) as a function of $K_{gb}$ (left) and average $N_T$ (right), for $I_T = 10$ and 100 nA. Differently from Fig. 5, the dependence on $K_{gb}$ appears similar but not the same for CTs and DTs, with power-law exponents of about 0.85 and 0.75, respectively. Note also that $\sigma_{V_T}$ is larger (by 19%) in the low-$K_{gb}$ limit but becomes smaller (by 14%) at the other extreme. When plotted as a function of $N_T$, a unique dependence is again obtained for both CT and DT models and both values of $I_T$, strengthening the role of $N_T$.

To verify the impact of traps on the average and rms $V_T$, we run simulations for a few cells, each having fixed GB configuration, and only changing number and positions of the traps. Results for five cells are reported in Fig. 7, together with previous average data for $I_T = 10$ nA: note that trap fluctuation in individual cells can lead to $V_T$ higher or lower than the average, but always returns a smaller spread, suggesting that $\sigma_{V_T}$ is mainly controlled by the randomness in GB number and position. Fig. 7 also allows to quantify the DT contribution to the spread for a given $N_T$: while CT cells feature negligible spread, a significantly higher value is achieved in the DT case, that however does not always translate into a higher $\sigma_{V_T}$.

### C. TEMPERATURE

Temperature ($T$) dependence of NAND string parameters has been investigated in several works [10], [32], [33], where the role of GBs has been discussed in a CT frame. Fig. 8 reports the $T$ dependence of the average and rms $V_T$, showing that the reduction in such quantities after a DT approach is more evident at low $T$, reaching about 20% for $T = 198$ K. This behavior can be understood referring to the single-GB device already considered in Fig. 4 (now with different random traps), and looking at the effect of temperature. Results are shown in Fig. 9, evaluated at the CT threshold condition for each temperature. The current density graph (top) makes clear that the non-uniformity induced by DTs is stronger at low $T$, while the profile tends to become more uniform and similar to the CT case as $T$ increases. This means that a larger difference in current, hence in $V_T$ and $N_T$, is expected at low $T$ between the CT and DT case.

Localized peaks in the current density are a consequence of the $E_c$ profile, as the Fermi levels (not shown) do not change significantly moving from CTs to DTs (see for example [19], [22]). The bottom figure confirms that dis-uniformity grows stronger at low $T$, enhancing percolation. Another feature that can be noted from this figure is that the positions of the $E_C$ peaks, located at charged DT sites, change with $T$ (see for example the region around 270 – 315°): trap number and position change with $T$, leading to a spread in the $V_T$ temperature dependence and to enhanced cross-temperature effects [34]. Such effects are detailed in

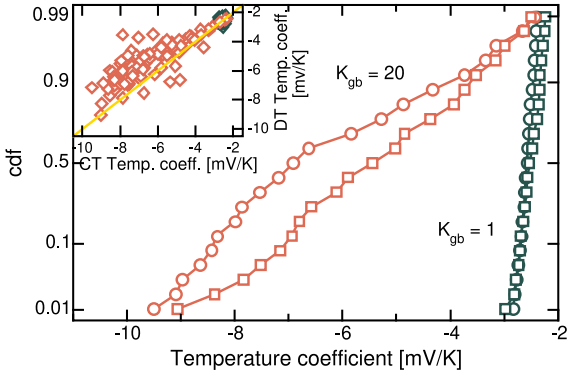


**FIGURE 10.** Temperature coefficients $\Delta V_T/\Delta T$ between 248 and 348 K for $K_{gb} = 1$ and 20. Circles = CTs, squares = DTs. Inset shows a cell-to-cell comparison of the coefficients, with the line marking equal values.

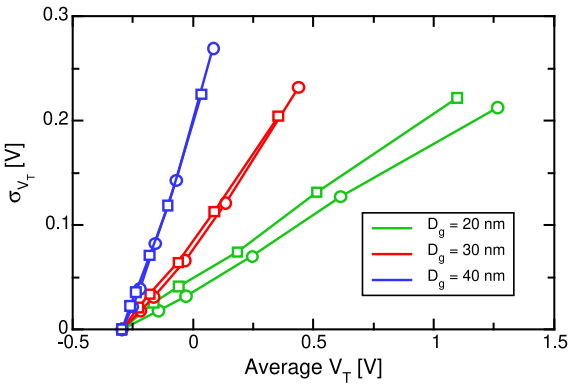


**FIGURE 11.** Rms $V_T$ as a function of its average value for different values of the grain size $D_g$. Circles = CTs, squares = DTs.

Fig. 10, where the CT and DT cdfs of the $V_T$ temperature coefficient $\Delta V_T/\Delta T$ (evaluated between 248 and 348 K) are compared. Note that CT and DT data are similar for $K_{gb} = 1$, but their separation increases with the trap density, leading to lower coefficients in the DT case. This is also highlighted in the inset, where a cell-to-cell comparison of the coefficients is reported: with few exceptions, DT coefficients at large $K_{gb}$ lie above the straight line that marks equal values. Finally, it is worth pointing out that these results have been obtained with a constant-mobility model, and could be affected by the adoption of more refined approaches, such as those in [10], [12].

## IV. DISCUSSION

In the previous Section, we have investigated the physics behind the different results obtained from a CT or DT approach, showing that a discrete treatment of traps results in different values of the average and rms $V_T$. However, the results also highlighted that when such quantities are plotted versus $N_T$, similar behaviors arise. It is then worthwhile to investigate whether DT effects can be described by a CT model via a change in the trap density, or not. To this aim, Fig. 11 shows the relation between the average $V_T$ and $\sigma_{V_T}$ in the investigated range of $K_{gb}$, for the nominal case (red),

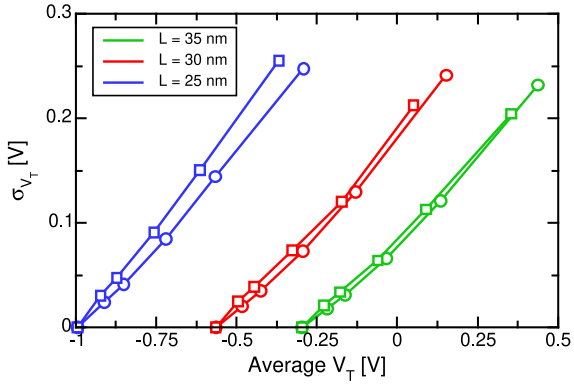


**FIGURE 12.** Rms $V_T$ as a function of its average value for different values of the cell length $L$. Circles = CTs, squares = DTs.

and two other conditions where the grain size $D_g$ has been changed. The general $V_T$ trend is similar to what reported in [15], [17], and is due to the fact that, in changing $D_g$, we have not modified the values of the GB trap density adopted in the default case, as done for example in [10]. This means that when $D_g$ is reduced and we have more GBs in the polysilicon, we get more occupied traps and higher $V_T$. More interestingly, we note that CT and DT results lie on the same curve for $D_g = 40$ nm, but diverges for smaller values. This means that in the former case, DT effects can indeed be described via a tailoring of the trap density by a factor of up to about 19% in the investigated range. However, this is no longer true for smaller $D_g$, where the curves diverge.

Similar data, now for different values of the channel length $L$, are shown in Fig. 12. Note that DT and CT curves tend to diverge in short channels, where the impact of charge discretization is larger. This proves again that a full DT approach is needed whenever a reliable analysis of device variability and its dependence on physical and architectural parameters is to be carried out.

## V. CONCLUSION

We have studied the impact of a discrete-trap approach on polysilicon channel 3-D NAND variability. Discrete-trap simulation leads to lower average and rms $V_T$ values, explained in terms of the different electrostatics and filled traps, as well as the stronger impact of a discrete charge on the conduction-band energy landscape. This means that CT results cannot be simply considered as an average of many DT cases. The effects are then investigated as a function of the cell parameters. The differences between the approaches show that discrete-trap modeling can improve the accuracy of device variability simulations.

## APPENDIX

As outlined in Section III.B, we briefly discuss the validity and limitations of our GB trap parameters. At its highest value, $K_{gb} = 20$ means that the areal GB trap density is about $1.2 \times 10^{15}$ cm$^{-2}$, which might be considered excessive if not unreasonable. An easy response could be that the trend

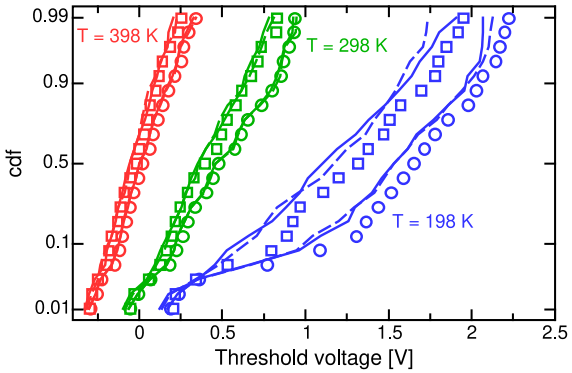


**FIGURE 13.** $V_T$ cdfs for different temperatures and $K_{gb} = 20$ in the nominal case (symbols: Circles = CTs, squares = DTs) and when the tail state density is not scaled with $K_{gb}$ (lines) or is zero (dashes).

**TABLE 1.** Parameters used in the sensitivity analysis.

| | Low energy | Nominal | High energy |
|---|---|---|---|
| $E_t$ [meV] | 11 | 16.6 | 24.9 |
| $D_t$ [cm$^{-3}$ eV$^{-1}$] | $5.3 \times 10^{15}$ | $3.53 \times 10^{15}$ | $2.35 \times 10^{15}$ |
| $E_d$ [meV] | 107 | 160.6 | 240.9 |
| $D_d$ [cm$^{-3}$ eV$^{-1}$] | $1.07 \times 10^{13}$ | $7.16 \times 10^{12}$ | $4.77 \times 10^{12}$ |

in the differences between CTs and DTs would not change if the $K_{gb}$ range were – say – limited to 10 or extended to 30, but there is one more reason that we would like to point out, and is that – owing to the low value of $E_t$ – the tail state density disappears below the deep states one about 115 meV below the CB edge and is expected to have little impact on our results, where $V_T$ is evaluated at 10 nA. To verify this statement, we run simulations where the tail state density $D_t$ is either zero or kept at its nominal value, while $K_{gb}$ only multiplies $D_d$, whose trap density becomes $2.3 \times 10^{13}$ cm$^{-2}$ at $K_{gb} = 20$. Fig. 13 shows previous results for $V_T$ cdfs at 198, 298, and 398 K (symbols), compared against the new ones (lines and dashes): notwithstanding the large difference in the total trap density, differences in $V_T$ are negligible at room or higher $T$, and grow slightly at 198 K, where the Fermi level approaches the CB. Note also that this choice does not affect the CT-DT difference, supporting the validity of all our results. In other words, the value of the tail state density has no impact on our results, and the deep-state one only should be considered as the trap density.

We conclude this Section with a sensitivity analysis on the trap parameters. To this aim, we repeated our simulations multiplying/dividing the energy parameters by a factor of 1.5, and scaling the peak density inversely, so to keep the total number of traps constant (see values in Table 1). Results for the average $V_T$ are summarized in Fig. 14: all CT and DT data follow the same trend, with a reduction in the average $V_T$ due to trap discretization. Furthermore, all data collapse onto the same curve when plotted as a function of $N_T$. A similar conclusion can be drawn for $\sigma_{V_T}$ (not shown), confirming that the physical picture we have proposed is not dependent on the details of the trap distribution.

Fig. 15 shows instead the TCs for the cases considered and $K_{gb} = 20$. While absolute values of the TCs are affected by

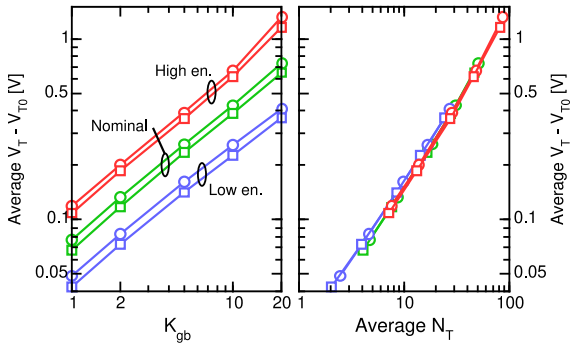


**FIGURE 14.** Same as Fig. 5, but with the addition of data from Table 1.

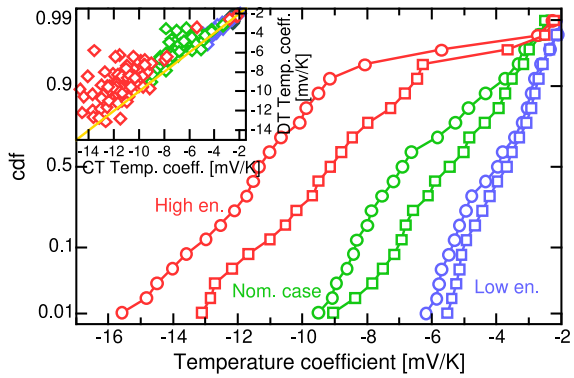


**FIGURE 15.** Same as Fig. 10 for $K_{gb} = 20$, but with the addition of data from Table 1.

the choice of the parameters and we have not investigated the dependence on $K_{gb}$ and $N_T$ to highlight the trends, the main conclusion remains: DT modeling leads to lower values for the TCs. Furthermore, the average percentage error between the two approaches changes from 17% in the nominal case to 19% in the high-energy one, showing little dependence, and only drops to 8% in the low-energy case.

## ACKNOWLEDGMENT

The authors would like to acknowledge many useful comments from an anonymous Reviewer.

## REFERENCES

[1] C. Monzio Compagnoni, A. Goda, A. S. Spinelli, P. Feeley, A. L. Lacaita, and A. Visconti, "Reviewing the evolution of the NAND Flash technology," *Proc. IEEE*, vol. 105, no. 9, pp. 1609–1633, Sep. 2017, doi: 10.1109/JPROC.2017.2665781.

[2] A. L. Lacaita, A. S. Spinelli, and C. M. Compagnoni, "High-density solid-state storage: A long path to success," in *Proc. IEEE Latin America Electron Devices Conf. (LAEDC)*, 2021, pp. 1–4, doi: 10.1109/LAEDC51812.2021.9437865.

[3] B. Kim et al., "A high-performance 1Tb 3b/cell 3D-NAND Flash with a 194MB/s write throughput on over 300 layers," in *ISSCC Dig. Tech.*, 2023, pp. 27–29, doi: 10.1109/ISSCC42615.2023.10067666.

[4] A. Khakifirooz et al., "1.67Tb, 5b/cell Flash memory fabricated in 192-layer floating gate 3D-NAND technology and featuring a 23.3Gb/mm$^2$ bit density," in *ISSCC Dig. Tech.*, 2023, pp. 400–401, doi: 10.1109/ISSCC42615.2023.10067616.

[5] K. Ishimaru, "Challenges of Flash memory for the next decade," in *Proc. IRPS*, 2021, pp. 279–283, doi: 10.1109/IRPS46558.2021.9405182.

[6] A. Spessot, C. Monzio Compagnoni, F. Farina, A. Calderoni, A. S. Spinelli, and P. Fantini, "Compact modeling of variability effects in nanoscale NAND Flash memories," *IEEE Trans. Electron Devices*, vol. 58, no. 8, pp. 2302–2309, Aug. 2011, doi: 10.1109/TED.2011.2147319.
[7] Y.-T. Oh et al., "Impact of etch angles on cell characteristics in 3D NAND Flash memory," *Microelectron. J.*, vol. 79, pp. 1–6, Sep. 2018, doi: 10.1016/j.mejo.2018.06.009.
[8] K. Ko, J. K. Lee, and H. Shin, "Variability-aware machine learning strategy for 3-D NAND Flash memories," *IEEE Trans. Electron Devices*, vol. 67, no. 4, pp. 1575–1580, Apr. 2020, doi: 10.1109/TD.2020.2971784.
[9] D. Lee and C. Shin, "Impact of stacking-up and scaling-down bit cells in 3D NAND on their threshold voltages," *Micromachines*, vol. 13, p. 1139, Jul. 2022, doi: 10.3390/mi13071139.
[10] D. Resnati et al., "Characterization and modeling of temperature effects in 3-D NAND Flash arrays—Part I: Polysilicon-induced variability," *IEEE Trans. Electron Devices*, vol. 65, no. 8, pp. 3199–3206, Aug. 2018, doi: 10.1109/TED.2018.2838524.
[11] C.-W. Yang and P. Su, "Simulation and investigation of random grain-boundary-induced variabilities for stackable NAND Flash using 3-D Voronoi grain patterns," *IEEE Trans. Electron Devices*, vol. 61, pp. 1211–1214, Apr. 2014, doi: 10.1109/TED.2014.2308951.
[12] R. Degraeve et al., "Statistical poly-Si grain boundary model with discrete charging defects and its 2D and 3D implementation for vertical 3D NAND channels," in *IEDM Tech. Dig.*, 2015, pp. 121–124, doi: 10.1109/IEDM.2015.7409636.
[13] A. Subirats et al., "Experimental and theoretical verification of channel conductivity degradation due to grain boundaries and defects in 3D NAND," in *IEDM Tech. Dig.*, 2017, pp. 517–520, doi: 10.1109/IEDM.2017.8268433.
[14] D. Verreck et al., "3D TCAD model for poly-Si channel current and variability in vertical NAND Flash memory," in *Proc. SISPAD*, 2019, pp. 61–64, doi: 10.1109/SISPAD.2019.8870494.
[15] T. Yang, Z. Xia, D. Shi, Y. Ouyang, and Z. Huo, "Analysis and optimization of threshold voltage variability by polysilicon grain size simulation in 3D NAND Flash memory," *IEEE J. Electron Devices Soc.*, vol. 8, pp. 140–144, Jan. 2020, doi: 10.1109/JEDS.2020.2970450.
[16] F. Wang, X. Zhan, Y. Li, and J. Chen, "Impacts of poly-si channel on cell variations in vertical scaled charge-trap (CT) 3D NAND Flash memory," in *Proc. ICSICT*, 2020, pp. 437–439, doi: 10.1109/ICSICT49897.2020.9278184.
[17] K. Nam, C. Park, J.-S. Yoon, G. Yang, M. S. Park, and R.-H. Baek, "Channel thickness and grain size engineering for improvement of variability and performance in 3-D NAND Flash memory," *IEEE Trans. Electron Devices*, vol. 69, no. 7, pp. 3681–3687, Jul. 2022, doi: 10.1109/TED.2022.3175681.
[18] P.-Y. Wang and B.-Y. Tsui, "A novel approach using discrete grain-boundary traps to study the variability of 3-D vertical-gate NAND Flash memory cells," *IEEE Trans. Electron Devices*, vol. 62, no. 8, pp. 2488–2493, Aug. 2015, doi: 10.1109/TED.2015.2438001.
[19] G. Nicosia et al., "Characterization and modeling of temperature effects in 3-D NAND Flash arrays—Part II: Random telegraph noise," *IEEE Trans. Electron Devices*, vol. 65, no. 8, pp. 3207–3213, Aug. 2018, doi: 10.1109/TED.2018.2839904.
[20] D. Verreck et al., "Quantitative 3-D model to explain large single trap charge variability in vertical NAND memory," in *IEDM Tech. Dig.*, 2019, pp. 755–758, doi: 10.1109/IEDM19573.2019.8993552.
[21] A. S. Spinelli, C. Monzio Compagnoni, and A. L. Lacaita, "Random telegraph noise in Flash memories," in *Noise in Nanoscale Semiconductor Devices*, T. Grasser, Ed., Cham, Switzerland: Springer, 2020, ch. 6, pp. 201–227.
[22] A. S. Spinelli, G. Malavena, A. L. Lacaita, and C. Monzio Compagnoni, "Random telegraph noise in 3D NAND Flash memories," *Micromachines*, vol. 12, no. 6, p. 703, 2021, doi: 10.3390/mi12060703.
[23] B. Song, H. Liu, L. Jin, X. Fu, F. Liu, and Z. Huo, "Impact of stacking layers on RTN in 3D charge trapping NAND Flash memory," *Microelectron. Rel.*, vol. 127, Dec. 2021, Art. no. 114415, doi: 10.1016/j.microrel.2021.114415.
[24] G. Malavena et al., "Discrete-trap effects on 3-D NAND variability—Part II: Random telegraph noise," *IEEE J. Electron Dev. Soc.*, vol. 12, pp. 658–661, 2024.
[25] S. M. Amoroso et al., "Understanding the impact of polysilicon percolative conduction on 3D NAND variability," in *Proc. SISPAD*, 2023, pp. 5.2.1–5.2.4, doi: 10.23919/SISPAD57422.2023.10319604.
[26] Y. Fukuzumi et al., "Optimal integration and characteristics of vertical array devices for ultra-high density, bit-cost scalable Flash memory," in *IEDM Tech. Dig.*, 2007, pp. 449–452, doi: 10.1109/IEDM.2007.4418970.
[27] *Sentaurus Process User's Manual V. V-2023.12*, Synopsys Inc., Mountain View, CA, USA, 2023.
[28] *Sentaurus Device User'S Manual V. V-2023.12*, Synopsys, Mountain View, CA, USA, 2023.
[29] *Garand VE User'S Manual Supplement for 3D-NAND V. V-2023.12*, SynopsysInc., Mountain View, CA, USA, 2023.
[30] M. D. Jacunski, M. S. Shur, and M. Hack, "Threshold voltage, field effect mobility, and gate-to-channel capacitance in polysilicon TFTs," *IEEE Trans. Electron Devices*, vol. 43, pp. 1433–1440, Sep. 1996, doi: 10.1109/16.535329.
[31] X. Jia et al., "Investigation of random telegraph noise under different programmed cell $V_t$ levels in charge trap based 3D NAND Flash," *IEEE Electron Dev. Lett.*, vol. 43, pp. 878–881, Jun. 2022, doi: 10.1109/LED.2022.3171176.
[32] D. Resnati, A. Goda, G. Nicosia, C. Miccoli, A. S. Spinelli, and C. Monzio Compagnoni, "Temperature effects in NAND Flash memories: A comparison between 2-D and 3-D arrays," *IEEE Electron Dev. Lett.*, vol. 38, pp. 461–464, Apr. 2017, doi: 10.1109/LED.2017/2675160.
[33] C. Zhao et al., "Investigation of threshold voltage distribution temperature dependence in 3D NAND Flash," *IEEE Electron Dev. Lett.*, vol. 40, no. 2, pp. 204–207, Feb. 2019, doi: 10.1109/LED.2018.2886345.
[34] C. Zambelli, L. Crippa, R. Micheloni, and P. Olivo, "Cross-temperature effects of program and read operations in 2D and 3D NAND Flash memories," in *Proc. IIRW*, 2018, pp. 44–47, doi: 10.1109/IIRW.2018.8727102.

Open Access funding provided by 'Politecnico di Milano' within the CRUI CARE Agreement